

# A COMPUTATIONAL STUDY OF LATERAL PHASE SEPARATION IN BIOLOGICAL MEMBRANES

VLADIMIR YUSHUTIN\*, ANNALISA QUAINI<sup>†</sup>, SHEEREEN MAJD<sup>‡</sup>, AND MAXIM  
OLSHANSKII<sup>§</sup>

**Abstract.** Conservative and non-conservative phase-field models are considered for the numerical simulation of lateral phase separation and coarsening in biological membranes. An unfitted finite element method is devised for these models to allow for a flexible treatment of complex shapes in the absence of an explicit surface parametrization. For a set of biologically relevant shapes and parameter values, the paper compares the dynamic coarsening produced by conservative and non-conservative numerical models, its dependence on certain geometric characteristics and convergence to the final equilibrium.

**Key words.** Surface Allen–Chan equation; Surface Cahn–Hilliard equation; Trace finite element method; Lateral phase separation.

**1. Introduction.** Over the past 20 years, there has been a growing interest in studying phase separation in cell membranes, mostly motivated by its important role in a variety of cellular processes. In fact, lipid-driven separation of immiscible liquid phases is likely a factor in the formation of rafts in cell membranes [77, 81]. Lipid rafts in eukaryotic cells have been associated with important biological processes, such as endocytosis, adhesion, signaling, and protein transport; see, e.g., [29]. Furthermore, lipid phase separation has recently been utilized to enhance the delivery performance of targeted lipid vesicles [9, 51]. The formation of reversible phase-separated (nano)patterns (resembling lipid-rafts) on the vesicle surface is expected to increase target selectivity, cell uptake and overall efficacy [9].

Phase separation and pattern formation in lipid bilayers has been studied theoretically, experimentally, and numerically. For theoretical investigations of the equilibrium configuration we refer to [4, 74, 52, 79, 47] and references therein. Experimental studies have been mostly conducted to visualize pattern formation on giant vesicles; see, e.g., [12, 81]. In particular, in [81] various dynamics have been observed with fluorescence microscopy, including domain ripening, spinodal decomposition, and viscous fingering. However, experimental investigations proved to be challenging due to the frail nature of giant vesicles. Computational studies help observe dynamics and gain insights that may not be obtained experimentally. Multicomponent vesicle have been investigated with different numerical approaches: molecular dynamics [65, 23], dissipative particle dynamics [56, 7], and continuum based methods [82, 62, 78, 69, 58, 40]. In this paper, we choose a continuum based method based on phase-field description.

The phase-field method has emerged as a powerful computational approach to modeling and predicting phase separation in materials and fluids. It describes the system using a set of conserved and/or non-conserved field variables that are continuous across the interfacial regions separating phases. The main reasons for the success of the phase-field methodology are two: it replaces sharp interfaces by thin transition

---

\*Department of Mathematics, University of Houston, Houston, Texas 77204 (yushutin@math.uh.edu).

<sup>†</sup>Department of Mathematics, University of Houston, Houston, Texas 77204 (quaini@math.uh.edu); Partially supported by NSF through grant DMS-1620384.

<sup>‡</sup>Department of Biomedical Engineering, University of Houston, Houston, Texas 77204 (smajd9@uh.edu); Partially supported by NSF through grant DMR-1753328.

<sup>§</sup>Department of Mathematics, University of Houston, Houston, Texas 77204 (molshan@math.uh.edu); Partially supported by NSF through grant DMS-1717516.

regions called diffuse interfaces, making front-tracking unnecessary; and it is based on rigorous mathematics and thermodynamics. We consider a diffuse-interface description of phase separation developed by Cahn and Hilliard in [16, 17] and by Allen and Cahn in [3]. The classical Cahn–Hilliard theory for phase transformation in closed systems is characterized by a conserved order parameter (concentration), while the Allen–Cahn equation describes the evolution of non-conserved order parameters during phase transformation. The Allen–Cahn and Cahn–Hilliard equations have been widely used in many complex moving interface problems in materials science and fluid dynamics through a phase-field approach; see, e.g., [63, 5, 14, 22, 60].

While there is still some controversy on the basis of lipid raft formation, function and even existence [68, 30], both conservative (Cahn–Hilliard) [66, 67, 39, 40, 41, 64] and non-conservative (Allen–Cahn, a.k.a. Landau–Ginzburg) [6, 33, 82, 34, 35] phase field models are considered in the literature for phase separation in lipid bilayers. By conservative it is meant that the model respects the conservation law for the phase concentration of species for any membrane surface element. In relation to this, we note that in experimental setting, a number of molecules are known to preferentially partition into one of lipid phases on phase-separated vesicles. Examples include membrane proteins caveolin-3, peripheral myelin protein 22 [11, 73] and membrane dyes [11, 13]. In such settings, the Cahn–Hilliard equation provides the correct model. Similarly, the conservative model seems to be suited to describe membrane separation in bacteria as well as mammalian cells. The use of a non-conservative model (Allen–Cahn equation) may be justified when phase separation induces “high” curvature to the membrane that leads to vesicle budding or basically formation and separation of individual vesicles from the original parent vesicle [12, 49]. We also note that a phase-field model with global volume constraints was proposed in [26, 2] for the modeling of an impermeable closed membrane embedded in an incompressible fluid. Finally, for additional models to simulate mobile lipid rafts we refer to [20, 21, 83, 1].

In this paper, we apply and critically compare both surface Cahn–Hilliard and surface Allen–Cahn equations for the numerical simulation of lateral phase separation in biological membranes. Some simplifying assumptions are made in the present study. First, we consider rigid shapes thus ignoring the coupling of lateral sorting to radial deformations caused by the minimization of elastic or bending energy (cf., e.g., [82, 34, 39, 35, 40]). Although most bio-membranes are compliant, the assumption is reasonable for some manufactured vesicles designed for intracellular drug delivery [55]. Second, we do not account here for possible viscous dissipation and fluidity of cell membrane (see, e.g., [64] for Cahn–Hilliard–Navier–Stokes surface models). Finally, we neglect the effect of an external fluid; see, e.g., [78] for modelling of a multicomponent vesicle in an external viscous flow.

The Allen–Cahn and Cahn–Hilliard equations are challenging to solve numerically due to non-linearity, and stiffness. The Cahn–Hilliard has the added difficulty of a fourth order derivative in space. Although there exists an extensive literature on numerical methods for these models in planar and volumetric domains (see, e.g., recent publications [46, 80, 61, 19, 48] and references therein), there are not so many papers where the equations are treated on surfaces. Solving equations numerically on general surfaces poses additional difficulties that are related to the discretization of tangential differential operators and the approximate recovery of complex shapes. Several authors have opted for a finite difference method. For example, the closest point finite difference method was applied to solve the surface Allen–Cahn equation in [53] and the Cahn–Hilliard equation on torus in [42] and in [50] on more general

domains. A finite difference method for a diffuse volumetric representation of the surface Cahn–Hilliard equation was introduced in [45]. A finite difference method in a reference domain was used in [40] to model phase separation with radial deformation on sphere like domains. However, a finite element method (FEM) is often considered to be the most flexible numerical approach to handle complex geometries.

Finite element solutions to the surface Allen–Cahn equation can be found in [27, 33, 35]. The convergence of a FEM for the surface Cahn–Hilliard equation was studied in [25], where numerical examples for a sphere and saddle surface are provided; the Cahn–Hilliard equation on more general surfaces was treated by a finite element method more recently in [41, 59]. Surface FEMs were extended to more general systems in several papers: in [69] solutions to the surface Cahn–Hilliard–Navier–Stokes equation were computed on a sphere and torus; the authors of [10] studied a finite element method for the bulk Navier–Stokes equations coupled to the surface Cahn–Hilliard model; and in [32] the Cahn–Hilliard equation was solved numerically by a finite element method on evolving surfaces. All of the above references use a sharp surface representation and a discretization mesh *fitted* to the computational surface.

In the present paper, we study for the first time a *geometrically unfitted* finite element method for the simulation of lateral phase separation on surfaces. Our approach builds on earlier work on a unfitted FEM for elliptic PDEs posed on surfaces [72] called TraceFEM. Unlike some other geometrically unfitted methods for surface PDEs, TraceFEM employs sharp surface representation. The surface can be defined implicitly and no knowledge of the surface parametrization is required. This approach allows for flexible numerical treatment of complex shapes, like the ones found in cell biology. After validating the accuracy of the numerical method with benchmark problems, we apply it to simulate phase transition on a series of surfaces of increasing geometric complexity using both the surface Allen–Cahn and Cahn–Hilliard models. The surfaces are chosen to resemble shapes of biological membranes known to exhibit phase separation. We compare the dynamic coarsening produced by conservative and non-conservative numerical models, its interplay with the curvature and convergence to the final equilibrium. An advantage of our approach is that it can handle “small” (of the order of 1% of the shape characteristic length, which is consistent with available experimental observations) interface thicknesses between phases without stability issues, as long as the time step is properly set. Finally, we note that TraceFEM can be naturally combined with a level-set surface representation and works well for PDEs posed on evolving surfaces, including cases with topological changes (cf., e.g., [57]). We will not make use of this rather unique property in this paper. However, such property will become very convenient for the numerical simulation of certain phenomena like uptake of drug carriers that use reversible phase-separated (nano)patterns on the vesicle surface [9, 51].

The remainder of the paper is organized as follows. In Sec. 2 we state the surface Allen–Cahn and the Cahn–Hilliard equations and the respective variational formulations. The application of TraceFEM to both models is presented in Sec. 3. After a validation of our implementation of TraceFEM, in Sec. 4 we study phase separation modeled by both the Allen–Cahn and the Cahn–Hilliard equations on different surfaces of increasing complexity. Concluding remarks are provided in Sec. 5.

**2. Mathematical model.** In order to state the surface Allen–Cahn and the Cahn–Hilliard equations, we first need to introduce some notation.

Let  $\Gamma$  be a closed sufficiently smooth surface in  $\mathbb{R}^3$ , with the outward pointing unit

normal  $\mathbf{n}$ . The surface represents a bio-membrane, e.g., a closed bilayer composed of multiple lipids, embedded in a bulk fluid. In the present study, we do not account for bulk phenomena and concentrate on the lateral behavior of the system. For any sufficiently smooth function  $g$  in a neighborhood of  $\Gamma$  its tangential gradient is defined as  $\nabla_{\Gamma}g = \nabla g - (\mathbf{n} \cdot \nabla g)\mathbf{n}$ . The tangential (surface) gradient  $\nabla_{\Gamma}g$  then depends only on values of  $g$  restricted to  $\Gamma$  and  $\mathbf{n} \cdot \nabla_{\Gamma}g = 0$  holds. For a vector field  $\mathbf{f}$  on  $\Gamma$  we define  $\nabla_{\Gamma}\mathbf{f}$  componentwise. We need the surface divergence operator for  $\mathbf{f}$  and the Laplace-Beltrami operator for  $g$  :

$$\operatorname{div}_{\Gamma}\mathbf{f} := \operatorname{tr}(\nabla_{\Gamma}\mathbf{f}), \quad \Delta_{\Gamma}g := \operatorname{div}_{\Gamma}(\nabla_{\Gamma}g),$$

where  $\operatorname{tr}(\cdot)$  is the trace of a matrix.

Further  $L^2(\Gamma)$  is the Lebesgue space of square-integrable functions on  $\Gamma$  and  $H^1(\Gamma)$  is the Sobolev space of all functions  $g \in L^2(\Gamma)$  such that  $\nabla_{\Gamma}g \in L^2(\Gamma)^3$ .

**2.1. Allen–Cahn equation.** Let  $\eta \in [0, 1]$  be an order parameter on  $\Gamma$ , i.e. a measure of the degree of order across the boundaries in a phase transition system, with  $\eta = 0$  indicating complete lack of order and  $\eta = 1$  indicating full order. Such parameter normally ranges between zero in one phase and nonzero in the other. For example, if solid-liquid phase transition happens on  $\Gamma$ , then the order parameter is the difference of the surface material densities. If the total specific free energy  $f$  is not at a minimum with respect to a local variation in  $\eta$ , Allen and Cahn postulated in [3] that there is an immediate change in  $\eta$  given by:

$$\frac{\partial \eta}{\partial t} = -\alpha \frac{\delta f}{\delta \eta} \quad \text{on } \Gamma \times (0, T], \quad (2.1)$$

where  $\alpha$  is a positive kinetic coefficient and  $(0, T]$  is the time interval of interest. The total specific (i.e., per unit surface) free energy  $f$  is a function of the order parameter:

$$f(\eta) = f_0(\eta) + \frac{1}{2}\epsilon^2|\nabla_{\Gamma}\eta|^2. \quad (2.2)$$

In (2.2),  $\epsilon$  is the gradient energy coefficient and  $f_0$  is the specific free energy of a homogeneous phase, which is a function of  $\eta$  with a characteristic double-well form. The kinetic equation (2.1) reflects the fact that the order parameter  $\eta$  is not a conserved quantity. The functional derivative of  $f$  with respect to  $\eta$  is given by:

$$\frac{\delta f}{\delta \eta} = f'_0(\eta) - \epsilon^2\Delta_{\Gamma}\eta. \quad (2.3)$$

Plugging (2.3) into eq. (2.1), we obtain:

$$\frac{\partial \eta}{\partial t} + \alpha f'_0(\eta) - \alpha\epsilon^2\Delta_{\Gamma}\eta = 0 \quad \text{on } \Gamma \times (0, T]. \quad (2.4)$$

We remark that  $\alpha\epsilon^2$  in eq. (2.4) has dimensions of a diffusion coefficient, i.e.  $\text{m}^2/\text{s}$ . Obviously, eq. (2.4) needs to be supplemented with initial condition  $\eta = \eta_0$  on  $\Gamma \times \{0\}$ , for a given  $\eta_0$ . A classical choice for  $f_0$  is the Ginzburg–Landau double-well potential

$$f_0(\eta) = \frac{1}{4}(\eta - 1)^2\eta^2,$$

which makes eq. (2.4) non-linear.

For the numerical method, we need a weak (variational) formulation of the surface Allen–Cahn equation. To devise it, one multiplies (2.4) by  $v \in H^1(\Gamma)$ , integrates over  $\Gamma$  and employs the integration by parts identity. For a closed smooth surface  $\Gamma$ , the integration by parts identity reads:

$$\int_{\Gamma} v \operatorname{div}_{\Gamma} \mathbf{f} \, ds = - \int_{\Gamma} \mathbf{f} \cdot \nabla_{\Gamma} v \, ds + \int_{\Gamma} \kappa v \mathbf{f} \cdot \mathbf{n} \, ds, \quad \text{for } \mathbf{f} \in H^1(\Gamma)^3, v \in H^1(\Gamma), \quad (2.5)$$

here  $\kappa$  is the sum of principle curvatures. Identity (2.5) is applied to the diffusion term in (2.4), i.e.  $\mathbf{f} = \nabla_{\Gamma} \eta$ , which makes the curvature term vanish. This leads to the weak formulation: Find  $\eta \in H^1(\Gamma)$  such that

$$\int_{\Gamma} \left( \frac{\partial \eta}{\partial t} + \alpha f'_0(\eta) \right) v \, ds + \alpha \epsilon^2 \int_{\Gamma} \nabla_{\Gamma} \eta \nabla_{\Gamma} v \, ds = 0, \quad \forall v \in H^1(\Gamma). \quad (2.6)$$

**2.2. Cahn–Hilliard equation.** On  $\Gamma$  we consider a heterogeneous mixture of two species with mass concentrations  $c_i = m_i/m$ ,  $i = 1, 2$ , where  $m_i$  are the masses of the components and  $m$  is the total mass. Since  $m = m_1 + m_2$ , we have  $c_1 + c_2 = 1$ . Let  $c_1$  be the representative concentration  $c$ , i.e.  $c = c_1$ . Unlike the order parameter  $\eta$  in Section 2.1, concentration  $c \in [0, 1]$  is a conserved quantity. Moreover let  $\rho$  be the constant total density of the system  $\rho = m/S$ , where  $S$  is the surface area of  $\Gamma$ . Phase separation in this two component system can be modelled by the Cahn–Hilliard equation [16, 17].

In order to describe the evolution of the concentration profile  $c(\mathbf{x}, t)$ , we consider the conservation law:

$$\rho \frac{\partial c}{\partial t} + \operatorname{div}_{\Gamma} \mathbf{j} = 0 \quad \text{on } \Gamma \times (0, T], \quad (2.7)$$

where  $\mathbf{j}$  is a diffusion flux. The flux  $\mathbf{j}$  is defined according to (empirical) Fick’s law:

$$\mathbf{j} = -M \nabla_{\Gamma} \mu \quad \text{on } \Gamma, \quad \mu = \frac{\delta f}{\delta c}, \quad (2.8)$$

where  $M$  is the so-called mobility coefficient (see [54]) and  $\mu$  is the chemical potential, which is defined as the functional derivative of the total specific free energy  $f$  with respect to the concentration  $c$ . Thus, we introduce the total specific free energy:

$$f(c) = f_0(c) + \frac{1}{2} \epsilon^2 |\nabla_{\Gamma} c|^2. \quad (2.9)$$

Just like in eq. (2.2),  $f_0(c)$  is the free energy per unit surface, while the second term represents the interfacial free energy based on the concentration gradient. We recall that in order to have phase separation,  $f_0$  must be a non-convex function of  $c$ . A fundamental fact of the chemical thermodynamics is that even when phase separation has occurred, there is a limited miscibility between the components. In model (2.7)–(2.9), the interface between the two components is a layer of size  $\epsilon$  where thermodynamically unstable mixtures are stabilized by a gradient term in the energy. Further details concerning the thermodynamics of partially miscible mixtures can be found, for example, in [54].

By combining eq. (2.7), (2.8), and (2.9), we obtain the surface Cahn–Hilliard equation:

$$\rho \frac{\partial c}{\partial t} - \operatorname{div}_{\Gamma} (M \nabla_{\Gamma} (f'_0 - \epsilon^2 \Delta_{\Gamma} c)) = 0 \quad \text{on } \Gamma. \quad (2.10)$$

Eq. (2.10) is a fourth-order equation, so casting it in a weak form would result in the presence of second-order spatial derivatives. From the numerical point of view, it is beneficial to avoid higher order spatial derivatives. Hence, it is common to rewrite eq. (2.10) in mixed form, i.e. as two coupled second-order equations:

$$\rho \frac{\partial c}{\partial t} - \operatorname{div}_\Gamma (M \nabla_\Gamma \mu) = 0 \quad \text{on } \Gamma, \quad (2.11)$$

$$\mu = f'_0 - \epsilon^2 \Delta_\Gamma c \quad \text{on } \Gamma. \quad (2.12)$$

System (2.11)–(2.12) needs to be supplemented with the definitions of mobility  $M$  and free energy per unit surface  $f_0$ . A possible choice for  $M$  is given by

$$M = M(c) = c(1 - c). \quad (2.13)$$

This mobility is referred to as a degenerate mobility, since it is not strictly positive. We note that in many of the existing analytic studies, as well as numerical simulations, mobility is assumed to be constant. At the same time, concentration dependent mobility was already considered by Cahn [17] and (2.13) is also a popular choice for numerical studies. Although it is known that the dependence between the mobility and the concentration difference produces important changes during the coarsening process, only a few authors consider more complex mobility functions; see, e.g., [87]. In the absence of studies on the appropriate mobility function for lateral phase separation in biological membranes, here we choose to use (2.13). Again, a common choice for  $f_0$  is given by

$$f_0(c) = \frac{\xi}{4} c^2 (1 - c)^2, \quad (2.14)$$

where  $\xi$  defines the barrier height, i.e. the local maximum at  $c = 1/2$  [36]. We set  $\xi = 1$  for the rest of the paper. With mobility as in (2.13) and specific free energy as in (2.14), problem (2.11)–(2.12) is a coupled system of nonlinear PDEs posed on  $\Gamma$ .

Following a procedure similar to the one used to get eq. (2.6), we obtain the weak (variational) formulation of the surface Cahn–Hilliard problem (2.11)–(2.12): Find  $(c, \mu) \in H^1(\Gamma) \times H^1(\Gamma)$  such that

$$\int_\Gamma \rho \frac{\partial c}{\partial t} v \, ds + \int_\Gamma M \nabla_\Gamma \mu \nabla_\Gamma v \, ds = 0, \quad (2.15)$$

$$\int_\Gamma \mu q \, ds - \int_\Gamma f'_0(c) q \, ds - \int_\Gamma \epsilon^2 \nabla_\Gamma c \nabla_\Gamma q \, ds = 0, \quad (2.16)$$

for all  $(v, q) \in H^1(\Gamma) \times H^1(\Gamma)$ .

**3. Numerical method.** Biological membranes exhibit asymmetric complex shapes, which may affect the phase separation on the bilayer in an intricate way. To model the process numerically, we apply the trace finite element method [71]. This method allows to solve for a scalar quantity or a vector field on the surface  $\Gamma$  and does not require parametrization or triangulation of  $\Gamma$ . To discretize surface equations, Trace-FEM relies on a tessellation of a bulk computational domain  $\Omega$  ( $\Gamma \subset \Omega$  holds) into shape regular tetrahedra untangled to the position of  $\Gamma$ .

Biological membranes also exhibit shape transitions and shape instabilities. Thus, a realistic model of phase separation on biological membranes requires to solve either the Allen–Cahn or Cahn–Hilliard equation on evolving shapes. This is our longer

term goal, which dictates the choice of the numerical approach. In fact, as already mentioned in Sec. 1, evolving surfaces with possible topology changes can be relatively easily handled in the present numerical framework [57].

Let the 3D bulk domain  $\Omega$  be such that  $\Gamma \subset \Omega$ . Surface  $\Gamma$  is defined implicitly as the zero level set of a sufficiently smooth (at least Lipschitz continuous) function  $\phi$ , i.e.  $\Gamma = \{\mathbf{x} \in \Omega : \phi(\mathbf{x}) = 0\}$ , such that  $|\nabla\phi| \geq c_0 > 0$  in a 3D neighborhood  $U(\Gamma)$  of the surface. The vector field  $\mathbf{n} = \nabla\phi/|\nabla\phi|$  is normal on  $\Gamma$  and defines quasi-normal directions in  $U(\Gamma)$ . Let  $\mathcal{T}_h$  be the collection of all tetrahedra, such that  $\bar{\Omega} = \cup_{T \in \mathcal{T}_h} \bar{T}$ . The subset of tetrahedra that have a *nonzero intersection* with  $\Gamma$  is denoted by  $\mathcal{T}_h^\Gamma$ . The grid is refined towards  $\Gamma$ , however the tetrahedra from  $\mathcal{T}_h^\Gamma$  form a quasi-uniform tessellation with the characteristic tetrahedra size  $h$ . The domain formed by all tetrahedra in  $\mathcal{T}_h^\Gamma$  is denoted by  $\Omega_h^\Gamma$ .

On  $\mathcal{T}_h^\Gamma$  we use a standard finite element space of continuous functions that are piecewise-polynomials of degree 1. Higher order finite elements are possible (see, e.g., [44]) but will not be addressed in this paper. This bulk (volumetric) finite element space is denoted by  $V_h$ ,

$$V_h = \{v \in C(\Omega_h^\Gamma) : v \in P_1(T) \text{ for any } T \in \mathcal{T}_h^\Gamma\}.$$

For the purpose of numerical integration, we approximate  $\Gamma$  with a “discrete” surface  $\Gamma_h$ , which is defined as the zero level set of a  $P_1$  Lagrangian interpolant for  $\phi$  on the one time refined mesh:

$$\Gamma_h = \{\mathbf{x} \in \Omega : \phi_h(\mathbf{x}) = 0, \quad \phi_h := I_{h/2}(\phi(\mathbf{x})) \in V_{h/2}\}, \quad \text{with } \mathbf{n}_h = \frac{\nabla I_{h/2}^2(\phi)}{|\nabla I_{h/2}^2(\phi)|},$$

where  $I_{h/2}^2(\phi)$  is a  $P_2$  nodal interpolant of the level set function. See Fig. 3.1.

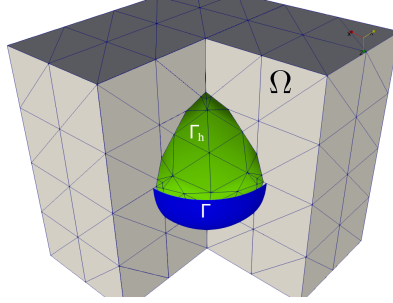


Fig. 3.1: Example of bulk domain  $\Omega$  with a given triangulation and sphere surface  $\Gamma$  with the corresponding “discrete” surface  $\Gamma_h$ .

For time-stepping we apply a semi-implicit stabilized schemes from [76]. At time instance  $t^k = k\Delta t$ , with time step  $\Delta t = \frac{T}{N}$ ,  $\eta^k$  denotes the approximation of the order parameter  $\eta(t^k, \mathbf{x})$ ; similar notation is used for other quantities of interest. Further, we need second order approximation of first and second time derivatives [76]:

$$[\eta]_t^k = \frac{3\eta^k - 4\eta^{k-1} + \eta^{k-2}}{2\Delta t}, \quad [\eta]_{tt}^k = \frac{\eta^{k+1} - 2\eta^k + \eta^{k-1}}{|\Delta t|^2}, \quad (3.1)$$

and linear extrapolation for  $f'_0$  at time  $t^k$ :  $\tilde{f}'_0(\eta)^k = 2f'_0(\eta^{k-1}) - f'_0(\eta^{k-2})$ . Same notations for differences and extrapolation will be used with other variables.

The finite element discretizations are based on the weak formulations of the surface Allen–Cahn and Cahn–Hilliard problems (2.6) and (2.15)–(2.16), respectively. For the Allen–Cahn equation, the semi-implicit stabilized TraceFEM reads: Given  $\eta_h^{k-1}, \eta_h^{k-2} \in V_h$ , find  $\eta_h^k \in V_h$  solving

$$\begin{aligned} \int_{\Gamma_h} \left\{ [\eta_h]_t^k + \beta_s |\Delta t|^2 [\eta_h]_{tt}^{k-1} + \alpha \tilde{f}'_0(\eta_h)^k \right\} v_h ds + \alpha \epsilon^2 \int_{\Gamma_h} \nabla_{\Gamma_h} \eta_h \cdot \nabla_{\Gamma_h} v_h ds \\ + \epsilon^2 h \int_{\Omega_h^\Gamma} (\mathbf{n}_h \cdot \nabla \eta_h^k)(\mathbf{n}_h \cdot \nabla v_h) dx = 0 \end{aligned} \quad (3.2)$$

for all  $v_h \in V_h$ ,  $k = 2, 3, \dots, N$ . For  $k = 1$  an obvious first order modification is used. The last term in (3.2) is included to stabilize the resulting algebraic systems [44]. The term is consistent up to geometric errors related to the approximation of  $\Gamma$  by  $\Gamma_h$  and  $\mathbf{n}$  by  $\mathbf{n}_h$  in the following sense: any smooth solution  $\eta$  of equations (3.2) can be always extended off the surface along (quasi)-normal directions so that  $\mathbf{n} \cdot \nabla \eta = 0$  in  $\Omega_h^\Gamma$ . Another stabilization term  $|\Delta t|^2 [\eta_h]_{tt}^{k-1}$  scaled with user defined parameter  $\beta_s$  is included to relax the stability restriction for the time step  $\Delta t$ . It introduces the consistency error of second order in time. We set  $\beta_s = 1$ .

Likewise, the semi-implicit stabilized TraceFEM for the Cahn–Hilliard equations (see Sec. 3.1.2 in [76]) reads: Given  $c_h^{k-1}, c_h^{k-2} \in V_h$  and  $\mu_h^{k-1}, \mu_h^{k-2} \in V_h$ , find  $c_h^k, \mu_h^k \in V_h$  solving

$$\begin{aligned} \int_{\Gamma_h} \rho [c_h]_t^k v_h ds + \int_{\Gamma_h} M(\tilde{c}^k) \nabla_{\Gamma_h} \mu_h^k \cdot \nabla_{\Gamma_h} v_h ds + h \int_{\Omega_h^\Gamma} (\mathbf{n}_h \cdot \nabla \mu_h^k)(\mathbf{n}_h \cdot \nabla v_h) dx \\ + \int_{\Gamma_h} \left\{ \mu_h^k - \beta_s |\Delta t|^2 [c_h]_{tt}^{k-1} - \tilde{f}'_0(c_h)^k \right\} q_h ds - \int_{\Gamma_h} \epsilon^2 \nabla_{\Gamma_h} c_h^k \nabla_{\Gamma_h} q_h ds \\ - \epsilon^2 h \int_{\Omega_h^\Gamma} (\mathbf{n}_h \cdot \nabla c_h^k)(\mathbf{n}_h \cdot \nabla q_h) dx = 0 \end{aligned} \quad (3.3)$$

for all  $v_h \in V_h$  and  $q_h \in V_h$ ,  $k = 2, 3, \dots, N$ . Again, for  $k = 1$  an obvious first order modification is used and we set  $\beta_s = 1$ .

The Allen–Cahn and Cahn–Hilliard equations define gradient flows of the energy functional  $E(u) = \int_{\Gamma} f(u) ds$  in  $L^2(\Gamma)$  and  $H^{-1}(\Gamma)$  (a dual space to  $H^1(\Gamma)$ ), respectively. More precisely, the following energy minimization properties hold:

$$\frac{d}{dt} E(\eta) = - \int_{\Gamma} \alpha |\epsilon^2 \Delta_{\Gamma} \eta + f'(\eta)|^2 ds < 0 \quad \text{Allen–Cahn} \quad (3.4)$$

$$\frac{d}{dt} E(c) = - \int_{\Gamma} |M(c) \nabla_{\Gamma} (\epsilon^2 \Delta_{\Gamma} c + f'(c))|^2 ds < 0 \quad \text{Cahn–Hilliard} \quad (3.5)$$

It is important for a physically consistent numerical method to adhere to fundamental properties (3.4) and (3.5). According to [76], the semi-discrete counterpart of (3.2) in a planar domain is stable with (slightly) modified potential  $\hat{f}_0$  such that  $\max_{x \in \mathbb{R}} |\hat{f}_0''| \leq L$  and under condition  $\Delta t \leq \frac{2}{3} L^{-1}$ . For the Cahn–Hilliard problem, the stability of a semi-discrete plain counterpart of (3.3) was shown for

$$\Delta t \leq \epsilon^2 L^{-2} \quad (3.6)$$

and  $M(c) = 1$ . A straightforward extension of arguments from [76] proves that the finite element solution to (3.2) is stable under the same condition and it holds:

$$E_h(\eta_h^{k+1}) \leq E_h(\eta_h^k) \quad \text{for all } k = 1, 2, \dots,$$



with the numerical energy functional,

$$E_h(\eta^k) = \int_{\Gamma_h} \alpha(f(\eta^k) + \beta_s |\Delta t|^2 |\eta]_{\tilde{t}}^k|^2) ds + \epsilon^2 h \int_{\Omega_h^\Gamma} |\mathbf{n}_h \cdot \nabla \eta^k|^2 dx,$$

here  $[\eta]_{\tilde{t}}^k := (\eta^k - \eta^{k-1})/\Delta t$  is the first order finite difference derivative. Extension of the stability analysis for the fully discrete method (3.3) with a concentration dependent mobility coefficient is less straightforward and we shall address it elsewhere. We remark that stability conditions are independent of  $\beta_s$ . It is, however, noted in [76] that in practice the restriction for time step is much less severe if stabilization parameter  $\beta_s$  is not too small. This also agrees with our numerical experience; see Sec. 4.2.3.

**4. Numerical experiments.** After validating the accuracy of the numerical method outlined in Sec. 3, a series of numerical tests is presented to study phase separation modeled by the Allen–Cahn and Cahn–Hilliard equations on surfaces of biological interest and to demonstrate the flexibility of our approach. We use free energy per unit surface (2.14) with  $\xi = 1$  for both equations for the sake of comparing the evolution of phase separations.

We start by comparing the numerical results produced by the two models on a sphere in Sec. 4.2. We find that the Cahn–Hilliard model successfully reproduces the spinodal decomposition experimentally observed in giant vesicles in [81]. Next, in Sec. 4.3 we compare both models on the surface of a spindle with the aim of getting a preliminary insight into the formation of microdomains in bacteria [15]. Finally, we present in Sec. 4.4 the results on a more complex surface that represents an idealized cell. For both the sphere and the idealized cell, we let the simulations run until sufficiently close to the steady state. All implementation are done in the FE package DROPS [24].

**4.1. Validation of the numerical method.** Before presenting the results on phase separation, we proceed with checking the spatial accuracy of the finite element method described in Sec. 3 with a benchmark test. The aim is to validate our implementation of the method. For this purpose, we consider the following synthetic solution to the Allen–Cahn equation on the unit sphere, centered at the origin:

$$\eta^* = \frac{1}{2} (1 - 0.8e^{-0.4t}) (Y(x_1, x_2) + 1), \quad Y(x_1, x_2) = x_1 x_2, \quad t \in [0, 5].$$

Here and in the following,  $\mathbf{x} = (x_1, x_2, x_3)^T$  denotes a point in  $\mathbb{R}^3$ . Thus,  $\eta^*$  is the exact solution to the non-homogeneous equation  $\eta_t + \alpha f'_0(\eta) - \alpha \epsilon^2 \Delta_\Gamma \eta = g$ , with free energy (2.14) and non-zero right-hand side  $g$ , which is easy to compute since  $Y$  is a real spherical harmonic function. We set  $\alpha = 1$  and  $\epsilon = 0.1$ .

To apply the method, we characterize the surface  $\Gamma$  as the zero level set of function  $\phi(\mathbf{x}) = \|\mathbf{x}\|_2 - 1$ , and embed  $\Gamma$  in an outer cubic domain  $\Omega = [-5/3, 5/3]^3$ . The initial triangulation  $\mathcal{T}_{h_\ell}$  of  $\Omega$  consists of 8 sub-cubes, where each of the sub-cubes is further subdivided into 6 tetrahedra. Further, the mesh is refined towards the surface, and  $\ell \in \mathbb{N}$  denotes the level of refinement, with the associated mesh size  $h_\ell = \frac{10/3}{2^{\ell+1}}$ . The refined tetrahedra cut by the surface form the computational mesh  $\mathcal{T}_{h_\ell}^\Gamma$ .

We report in Fig. 4.1 the discrete  $L_\infty(0, T; L^2(\Gamma_h))$  norm:

$$\|\eta^* - \eta_h\|_{\infty, 2} = \max_k \|\eta^*(t_k) - \eta_h(t_k)\|_{L^2(\Gamma_h)} \quad (4.1)$$

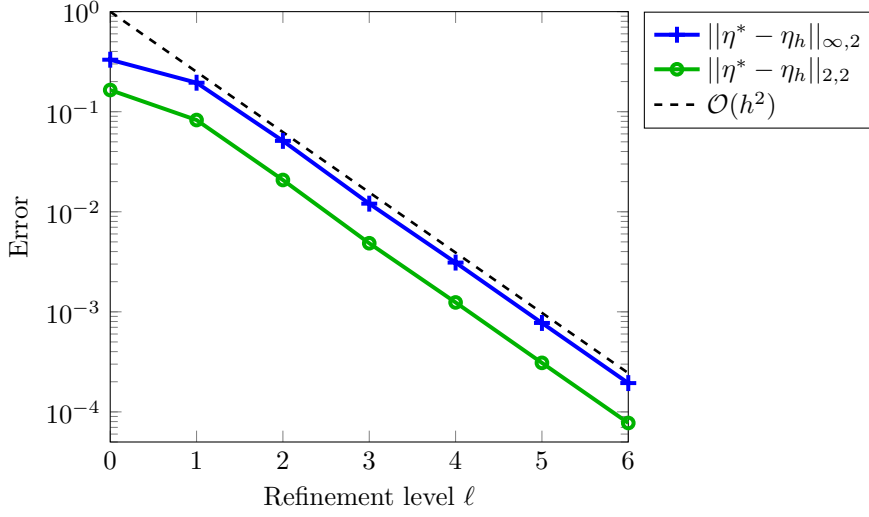


Fig. 4.1: Discrete  $L_\infty(0, T; L^2(\Gamma_h))$  norm (4.1) and discrete  $L_2(0, T; L^2(\Gamma_h))$  norm (4.2) of the error for order parameter  $\eta$  plotted against the refinement level  $\ell$  with  $\Delta t = 2^{-(1+\ell)}$ .

and the discrete  $L_2(0, T; L^2(\Gamma_h))$  norm:

$$\|\eta^* - \eta_h\|_{2,2} = \left( \frac{1}{T} \sum_k \Delta t \|\eta^*(t_k) - \eta_h(t_k)\|_{L^2(\Gamma_h)}^2 \right)^{1/2} \quad (4.2)$$

of the error for order parameter  $\eta$  plotted against the refinement level  $\ell$ . The time step was refined together with the mesh size according to  $\Delta t = 2^{-(1+\ell)}$ . Norms in (4.1)–(4.2) naturally appear in the error analysis for Allen–Cahn equation; see [76]. The second order convergence observed in Fig. 4.1 is optimal for  $P^1$  finite elements and consistent with the second order time-stepping method in (3.2). We note that all the norms reported in Fig. 4.1 are computed on the approximate surface  $\Gamma_h$ , where  $\eta^*$  was defined through its normal extension from  $\Gamma$ .

To assess the numerical solver for the Cahn–Hilliard model, we similarly consider the following exact solution to non-homogeneous surface Cahn–Hilliard equations with free energy per unit surface (2.14):

$$c^* = \frac{1}{2} (1 - 0.8e^{-0.4t}) (Y(x_1, x_2) + 1), \quad Y(x_1, x_2) = x_1 x_2, \quad t \in [0, 5],$$

i.e., same exact solution we used for order parameter in the Allen–Cahn equation. The exact chemical potential  $\mu^*$  can be readily computed from eq. (2.12). We set  $\rho = 1$ , mobility  $M$  as in (2.13), and  $\epsilon = 0.1$ .

We report in Fig. 4.2 the discrete  $L_\infty(0, T; L^2(\Gamma_h))$  norm (4.1) and discrete  $L_2(0, T; L^2(\Gamma_h))$  norm (4.2) of the error for concentration  $c$  (blue lines) and chemical potential  $\mu$  (red lines) plotted against the refinement level  $\ell$ , with time step  $\Delta t = 2^{-(1+\ell)}$ . All the norms reported in Fig. 4.2 are computed on the approximate surface  $\Gamma_h$ , where  $c^*$  and  $\mu^*$  were defined through their normal extensions from  $\Gamma$ . As for the Allen–Cahn equation, we see optimal second order of convergence in the

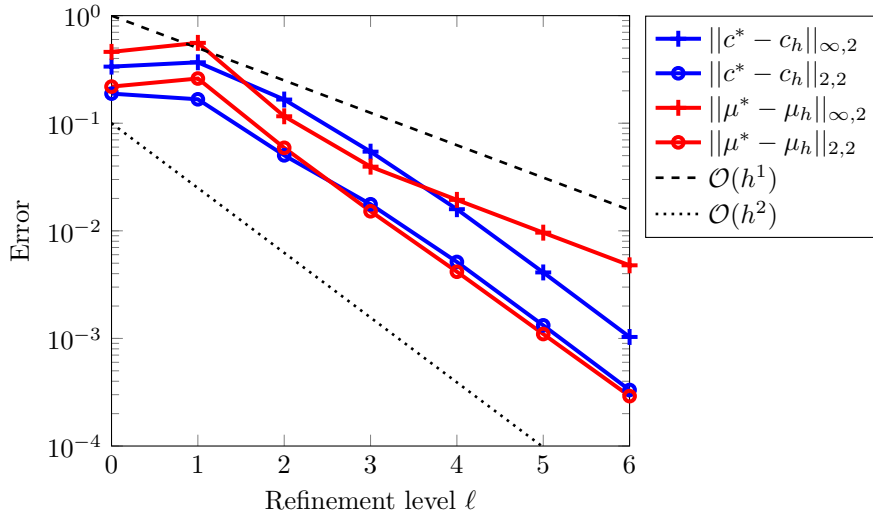


Fig. 4.2: Discrete  $L_\infty(0, T; L^2(\Gamma_h))$  norm (4.1) and discrete  $L_2(0, T; L^2(\Gamma_h))$  norm (4.2) of the error for concentration  $c$  (blue lines) and chemical potential  $\mu$  (red lines) plotted against the refinement level  $\ell$  with time step  $\Delta t = 2^{-(1+\ell)}$ .

discrete  $L_2(0, T; L^2(\Gamma_h))$  norm for both variables. In the discrete  $L_\infty(0, T; L^2(\Gamma_h))$  norm, the concentration converges to the exact solution with the second order, while chemical potential converges with first order. Note that the definition of the chemical potential involves the derivatives of the concentration and hence the loss of convergence order can be anticipated. Both convergence trends are consistent with the numerical analysis found in the literature for the planar Cahn–Hilliard equations; see, e.g., [31, Th.3.1], [76, Th.3.1], [38, Th.3]. The optimal convergence of concentration for the finite element approximations to surface Cahn–Hilliard was shown also in [25, 32], while for the discrete chemical potential only boundedness was shown.

In the convergence tests above, we used  $\epsilon = 0.1$ . The quantity  $\epsilon$  is a crucial modeling parameter, since it defines the thickness of a layer where phase transition takes place. The ability of method to resolve this interfacial phenomena is critical for the physical fidelity of the simulations. The case of smaller  $\epsilon$  is numerically challenging as seen, for example, from stability restriction (3.6) and the blow-up of known error estimates for  $\epsilon \rightarrow 0$  [38, 76]. To ensure that the interfacial region is properly resolved (i.e. enough elements fit in its thickness), it is common to apply mesh adaptivity techniques; see, e.g., [85, 8, 69]. We will not address mesh adaptivity in this paper. Therefore, we need to make sure that the finer meshes we consider are suited for thin interfacial regions such as the ones for  $\epsilon = 0.02, 0.01$ . Notice that these are realistic values of  $\epsilon$ . In fact, if we consider a typical giant vesicle with an average diameter of  $30 \mu\text{m}$ , on which phase separation can be visualized using fluorescence microscopy [81] with a resolution of about  $300 \text{ nm}$ , the thickness of transition region between the phases is approximately 1% of vesicle diameter.

For this purpose, we consider the eq. (2.4) with free energy per unit surface (2.14) and initial condition is  $\eta_0(\mathbf{x}) = x_3 + 1/2$ . We let the simulation run until changes in the interface thickness cannot be visually appreciated. Fig. 4.3 show a magnified view of the interface thickness at  $t = 30$  for  $\epsilon = 0.02$  and meshes  $\ell = 5, 6$ , and at

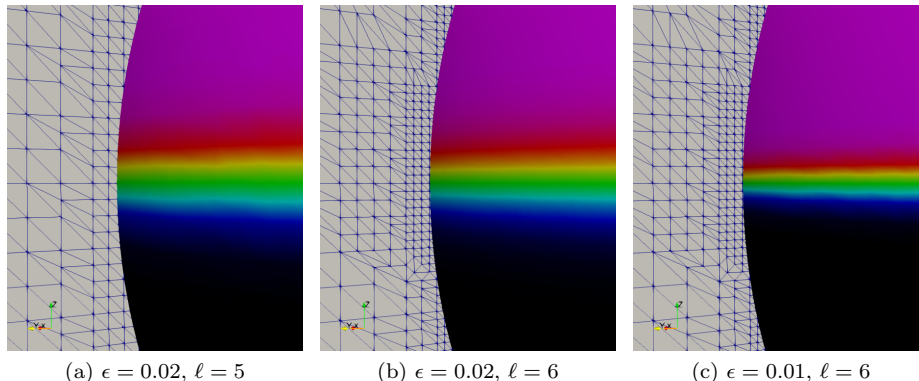


Fig. 4.3: Magnified view of the interface thickness and bulk mesh near  $\Gamma$  for (a)  $\epsilon = 0.02$  and mesh  $\ell = 5$ , (b)  $\epsilon = 0.02$  and mesh  $\ell = 6$ , and (c)  $\epsilon = 0.01$  and mesh  $\ell = 6$ .

$t = 60$  for  $\epsilon = 0.01$  and mesh  $\ell = 6$ , together with the bulk mesh near the surface. From Fig. 4.3 (a) and (b), we see that the thickness of the computed interface does not vary significantly from mesh  $\ell = 5$  to mesh  $\ell = 6$ , indicating that both meshes are sufficiently refined for  $\epsilon = 0.02$ . Fig. 4.3 (b) and (c) show that the thickness of the interface computed with mesh  $\ell = 6$  gets halved when  $\epsilon$  goes from 0.02 to 0.01. Thus, we use mesh  $\ell = 6$  to perform all numerical simulation reported further.

**4.2. Phase separation on a sphere.** The surface of the sphere is appealing not only for its simplicity, which makes it ideal for benchmarking, but also for its relevance in practical applications. In fact, lipid vesicles used as drug carriers have a spherical shape [55]. Therefore, we first focus on the process of phase separation on the surface of the sphere.

We consider both Allen–Cahn and Cahn–Hilliard equations, i.e. eq. (2.4) and (2.10), with free energy per unit surface (2.14) and  $\epsilon = 0.01$ . The initial condition is still  $\eta_0(\mathbf{x}) = \text{rand}(\mathbf{x})$ . Notice that this initial state corresponds to having a single thermodynamic phase, i.e. a “homogeneous” mix of the components. This miscible chemical mixture is unstable and proceed to separate into two distinct phases by diffusion. This process is characterized by two time scales: an initial fast stage followed by a slower process. In fact, the minimization of the chemical energy results in very fast development in the early stage of the phase separation. Later on, in the coarsening process, the dissipation of the interfacial energy is orders of magnitude slower.

**4.2.1. Allen–Cahn model.** The evolution of the numerical solution to the Allen–Cahn equation for  $t \in (0, 400]$  is shown in Fig. 4.4. We see that after the initial fast stage, which ends in a little more than ten time units, there is a considerable slow down in the evolution of the solution. The separation into two regions, one pink region with  $\eta = 1$  and one black region with  $\eta = 0$ , happens around  $t = 800$ . Fig. 4.5 displays the evolution of the numerical solution of the Allen–Cahn equation for  $t \in [1060, 12060]$ , i.e. after the separation into two regions has occurred. We notice a further deceleration in the process of dissipation of the interfacial energy. Finally, Fig. 4.6 shows how the solution evolves until one phase (the pink one) disappears at

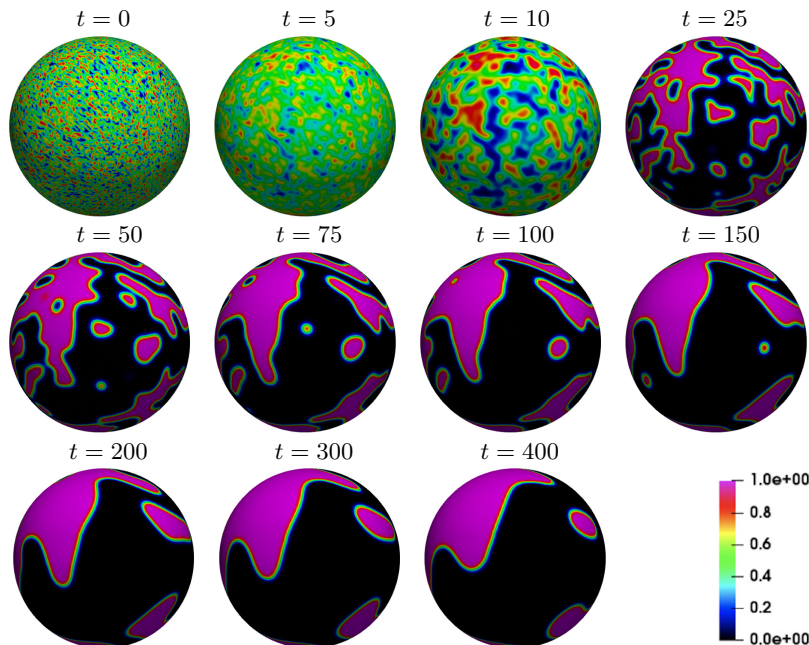


Fig. 4.4: Evolution of the numerical solution of the Allen–Cahn equation on the sphere for  $t \in (0, 400]$  computed with mesh  $\ell = 6$  and time step as specified in Table 4.1. The simulation was started with a random initial condition depicted in the top left panel. View:  $xy$ -plane.

around  $t = 22560$ . We recall that the Allen–Cahn equation describes the evolution of a non-conserved order parameter during phase transformation. Thus it is expected that one phase vanishes on the sphere, since it is not possible to trace a curve of minimal length on its surface, i.e. there is no minimal length interface (cf. Sec. 4.4). As we will see next, this is not the case when phase separation on the sphere is modeled by the Cahn–Hilliard equation.

Fig. 4.4, 4.5, and 4.6 clearly show the different time scales involved in the phase separation process modeled by the Allen–Cahn equation. In order to follow it, we prescribe different time steps for the different stages. Table 4.1 reports the time step assigned to each time interval. It would be less intrusive to use some time-adaptivity strategy [46, 75], which will be addressed in a forthcoming paper.

interval	(0, 10]	(10, 60]	(60, 1060]	(1060, 3560]	(3560, 13560]	(13560, 22560]
$\Delta t$	1	5	10	50	100	200

Table 4.1: Time steps used for the different time intervals to obtain the results in Fig. 4.4, 4.5, and 4.6.

**4.2.2. Cahn–Hilliard model.** Fig. 4.7 shows the evolution of the numerical solution to the Cahn–Hilliard problem for  $t \in (0, 500]$ . We see that during the initial stage a pattern forms much faster than in the evolution modeled by the Allen–Cahn equation. In fact from Fig. 4.7 we observe the emergence of a pattern already at time

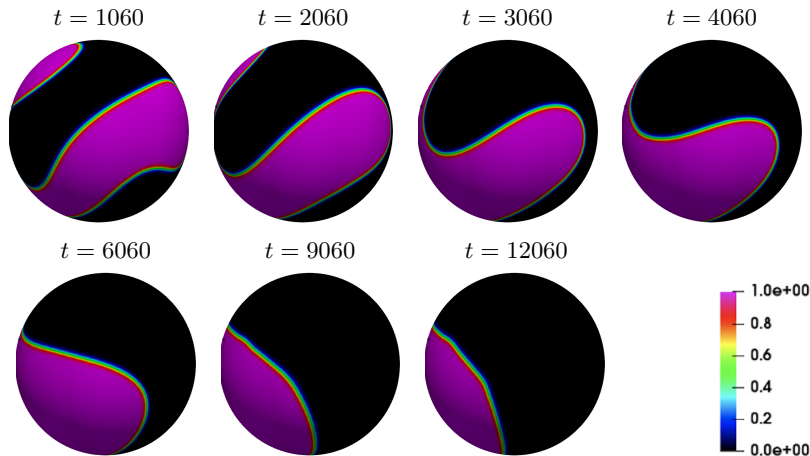


Fig. 4.5: Evolution of the numerical solution of the Allen–Cahn equation on the sphere for  $t \in [1060, 12060]$ , i.e. after the separation into two regions has occurred, computed with mesh  $\ell = 6$  and time step as specified in Table 4.1. View:  $yz$ -plane.

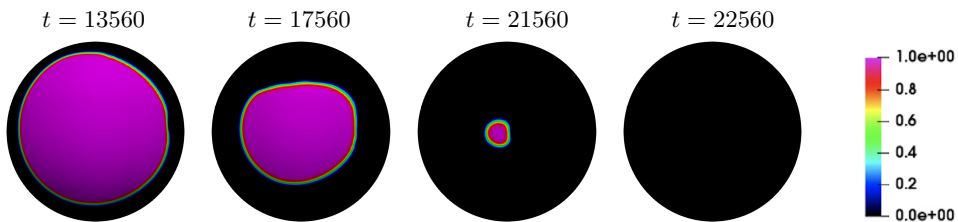


Fig. 4.6: Evolution of the numerical solution of the Allen–Cahn equation on the sphere for  $t \in [13560, 22560]$  computed with mesh  $\ell = 6$  and time step as specified in Table 4.1. Angled view of the  $xz$ -plane.

$t = 0.5$ , while Fig. 4.4 shows no pattern yet at  $t = 5$ . We recall that we have used the same free energy  $f_0$  for both the Allen–Cahn and Cahn–Hilliard models. Because of this difference in the early stage, Fig. 4.4 and 4.7 display solutions computed at different times. Also in the evolution given by the Cahn–Hilliard equation, we observe a considerable slow down after the initial fast stage, which ends around  $t = 1$ . After  $t = 50$ , the process of dissipation of the interfacial energy seems to slow down even further.

Fig. 3 (b) in [81] shows the spinodal decomposition observed experimentally in a vesicle that has a 1:1 concentration of DOPC (an unsaturated lipid)/DPPC (a saturated phospholipid) with 35% cholesterol. This ternary mixture at a certain temperature gives rise to separation into two phases: a dark, liquid-ordered phase that is rich in DPPC and cholesterol, and a bright, less ordered phase that is rich in DOPC. The panels in Fig. 4.7 associated to  $t = 0.5, 1, 10$  resemble the images in Fig. 3 (b) in [81], indicating that the Cahn–Hilliard equation provides a possible model for spinodal decomposition in vesicles.

The evolution of the numerical solution to the Cahn–Hilliard problem for  $t \in [1000, 25000]$  is shown in Fig. 4.8. We see that little changes in the solution occur

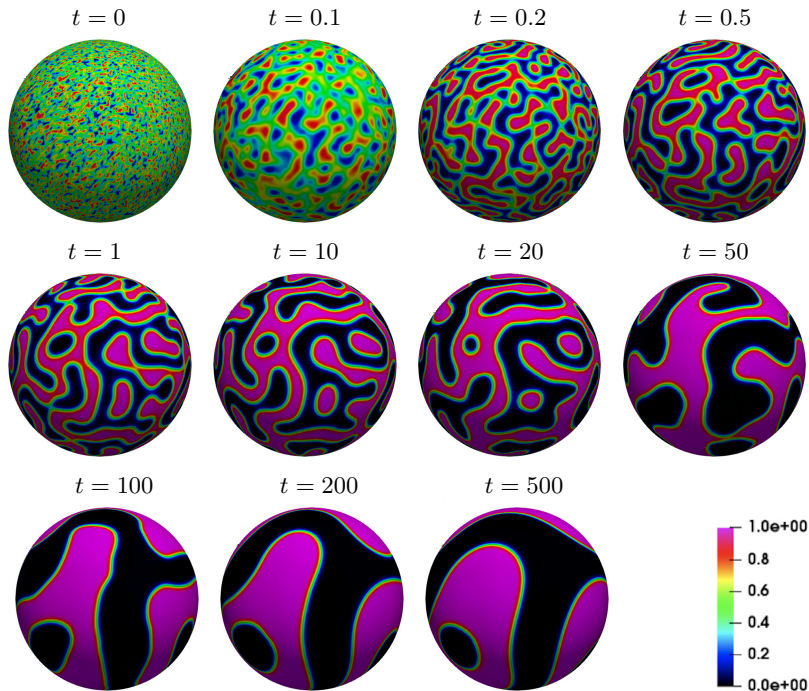


Fig. 4.7: Evolution of the numerical solution of the Cahn–Hilliard equation on the sphere for  $t \in (0, 500]$  computed with mesh  $\ell = 6$ . Time step is  $\Delta t = 0.01$  for  $t \in (0, 1]$  and  $\Delta t = 1$  for  $t \in (1, 500]$ . View:  $yz$ -plane.

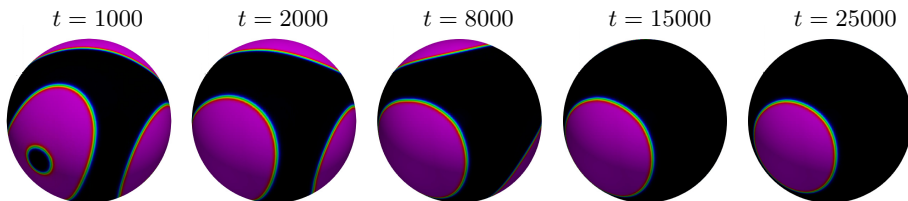


Fig. 4.8: Evolution of the numerical solution of the Cahn–Hilliard equation on the sphere for  $t \in [1000, 25000]$  computed with mesh  $\ell = 6$  and time step  $\Delta t = 1$ . View:  $yz$ -plane. The legend is as in Fig. 4.7

between  $t = 15000$  and  $t = 25000$ . After  $t = 25000$ , there is no visible change in the position of the interface between phases. In order to give a better idea of the equilibrium, we show another view of the solution for  $t \in [16000, 25000]$  in Fig. 4.9. Close to the steady state, we observe one large and one small pink domain (i.e.,  $c = 1$ ). We recall that the specific free energy (2.14) for the Cahn–Hilliard equation is not convex, this being a necessary condition to have phase separation. Thus, more than one stable equilibrium might exist solely due to the definition of the specific free energy, not considering surface symmetries.

In order to follow the initial fast phase, we set  $\Delta t = 0.01$  for  $t \in (0, 1]$ . For the remaining part of the considered time interval  $\Delta t$  was set to 1. Obviously, also

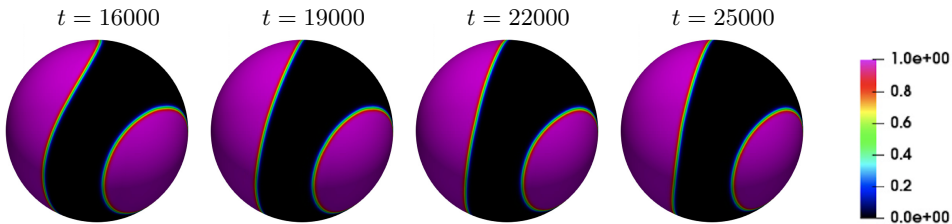


Fig. 4.9: Evolution of the numerical solution of the Cahn–Hilliard equation on the sphere for  $t \in [16000, 25000]$  computed with mesh  $\ell = 6$  and time step  $\Delta t = 1$ . View:  $xz$ -plane.

for the Cahn–Hilliard problem a time-adaptivity strategy can be adopted. See, e.g., [84, 43, 86, 46]

**4.2.3. On stabilization parameter  $\beta_s$ .** The fully discrete problems (3.2) and (3.3) feature user defined stabilization parameter  $\beta_s$ . As a rule of thumb on how to set its value, in [76] it is suggested that  $\beta_s$  should not be “too small” in order to relax the severity of the restriction for time step that comes from the analysis. See also Sec. 3. In this section, we report some numerical results to further support the suggestion in [76].

Let

$$E_h^L(u_h) = \int_{\Gamma_h} f(u_h) ds = \int_{\Gamma_h} \left( f_0(u_h) + \frac{1}{2} \epsilon^2 |\nabla_{\Gamma} u_h|^2 \right) ds \quad (4.3)$$

be the discrete Lyapunov energy functional for the Allen-Cahn ( $u_h = \eta_h$ ) and Cahn–Hilliard ( $u_h = c_h$ ) problems. We consider again both problems posed on the unit sphere, with  $\epsilon = 0.01$ , and initial condition given by  $\text{rand}(\mathbf{x})$ . We let the value of  $\beta_s$  range from 0 to 10. Fig. 4.10 shows the evolution of  $E_h^L(\eta_h)$  over time for  $\Delta t = 10$ , while Fig. 4.11 displays the evolution of  $E_h^L(c_h)$  over time for  $\Delta t = 1$ . We see that the discrete Lyapunov energy functional blows up when  $\beta_s$  is small with respect to the time step, meaning  $\beta_s \leq 0.1$  for the Allen-Cahn problem and  $\beta_s \leq 0.28$  for the Cahn–Hilliard problem.

We remind the stability conditions in [76] are independent of  $\beta_s$ . The suggestion for the value of  $\beta_s$  comes from experimental practice. The numerical experiments in [76] refer to problems (3.2) and (3.3) in planar domains. The Cahn–Hilliard problem in [76] is simplified by setting mobility to 1. The results reported in Fig. 4.10 and 4.11 show that the rule of thumb suggested in [76] holds also for non-planar surfaces and concentration dependent mobility.

**4.3. Phase separation on a spindle surface.** The surface  $\Gamma$  is given by the zero of the level set function

$$\phi(\mathbf{x}) = \begin{cases} \cos^2\left(\frac{x_1\pi}{10}\right) - (4x_2)^2 - (4x_3)^2 & \text{if } x_1 < 5 \\ -25 & \text{if } x_1 > 5 \end{cases}.$$

This corresponds to the surface of a spindle with maximum radius 0.25. We consider this surface because it resembles that of the bacteria studied in [15]. The surface  $\Gamma$  is embedded in an outer domain  $\Omega = [-5, 5] \times [-4/3, 4/3] \times [-4/3, 4/3]$ . A computational mesh  $\mathcal{T}_h^{\Gamma}$  is generated with mesh size  $h = 0.026$ . This is a level of refinement



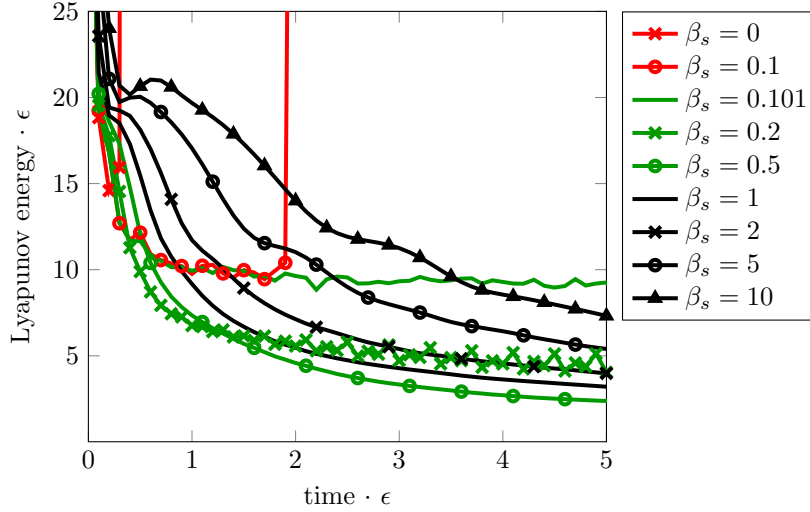


Fig. 4.10: Evolution of the discrete Lyapunov energy functional (4.3) for the Allen–Cahn problem (3.2) posed on the unit sphere with random initial data,  $\epsilon = 0.01$ ,  $\Delta t = 10$ , and different values of stabilization parameter  $\beta_s$ .

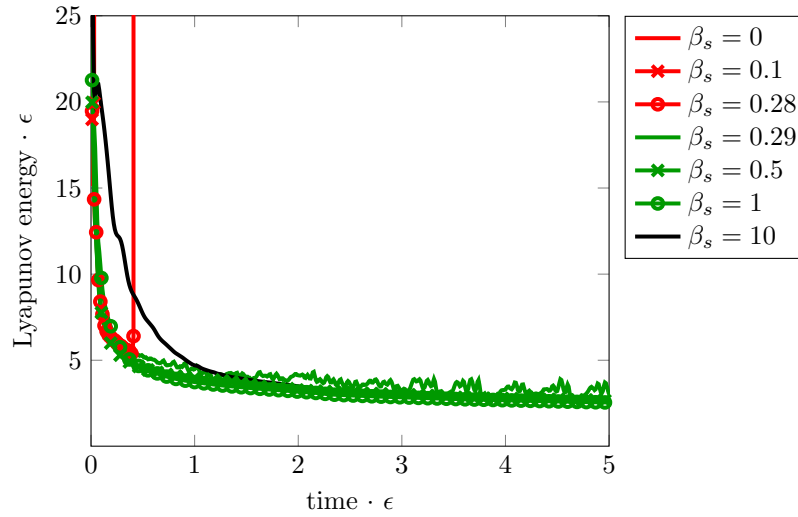


Fig. 4.11: Evolution of the discrete Lyapunov energy functional (4.3) for the Cahn–Hilliard problem (3.3) posed on the unit sphere with random initial data,  $\epsilon = 0.01$ ,  $\Delta t = 1$ , and different values of stabilization parameter  $\beta_s$ .

comparable to mesh  $\ell = 6$  in Sec. 4.1, which we have seen is appropriate for interface thickness  $\epsilon = 0.01$  or bigger.

In [15], it is reported that bacteria organize many processes in functional membrane microdomains equivalent to the lipid rafts. Thus, we simulate phase separation on the spindle using both models, i.e. eq. (2.4) and (2.10), with free energy per unit

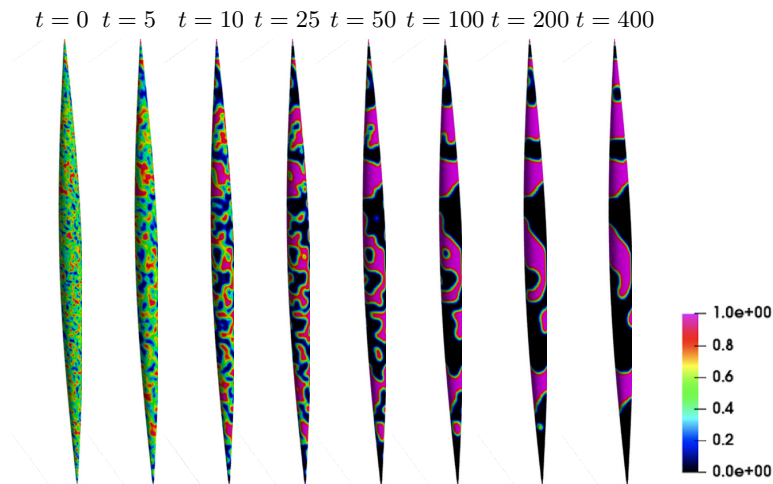


Fig. 4.12: Evolution of the numerical solution of the Allen–Cahn equation on the spindle for  $t \in (0, 400]$  computed with time step  $\Delta t = 1$  and on a mesh with size  $h = 0.026$ . The simulation was started with a random initial condition depicted in the leftmost panel. View:  $xy$ -plane.

surface (2.14),  $\alpha = 1$ , and  $\epsilon = 0.01$ . The initial condition is  $\eta_0(\mathbf{x}) = \text{rand}(\mathbf{x})$ , where  $\text{rand}(\mathbf{x})$  is a uniformly distributed random number between 0 and 1.

**4.3.1. Allen–Cahn model.** Fig. 4.12 shows the evolution of the numerical solution of the Allen–Cahn equation computed with the mesh described above and  $\Delta t = 1$ . Again, we observe that the initial fast stage ends after a little after 10 time units and then the evolution of the solution slows down considerably. Fig. 1 in [15] shows a heterogeneous distribution in the cytoplasmic membrane of bacillus subtilis, displaying a punctate pattern along the entire cell which qualitatively resembles the rightmost panel in Fig. 4.12. We would like to stress that the rightmost panel in Fig. 4.12 does not correspond to a steady state of the solution to the Allen–Cahn equation. In fact, if we were to let the simulation continue, it would evolve towards the disappearance of one phase as observed on the sphere in Sec. 4.2.

**4.3.2. Cahn–Hilliard model.** The evolution of the numerical solution to the Cahn–Hilliard equation for  $t \in (0, 400]$  is shown in Fig. 4.13. Just like on the sphere, a pattern emerges as early as  $t = 0.5$ . In order to follow this fast initial phase, we choose the same time steps as for the sphere, i.e.  $\Delta t = 0.01$  for  $t \in [0, 1]$  and  $\Delta t = 1$  for  $t > 1$ .

In order to compare phase separation on the spindle modeled by the Allen–Cahn and Cahn–Hilliard equations, we point out that Fig. 4.12 and 4.13 display solutions computed at different times. Although we see a faster and more ordered separation of phases from the Cahn–Hilliard model, the solutions computed with both models at time  $t = 400$  are not significantly different in terms of surface area occupied by each phase. Compare the rightmost panels in Fig. 4.12 and 4.13. So, from these preliminary results it is not possible to conclude which model is better suited to simulate the formation of microdomains in the cytoplasmic membrane of bacillus subtilis. Further investigation is needed. In addition, the role played by the initial condition that has to be understood, since in our tests on the spindle we have not

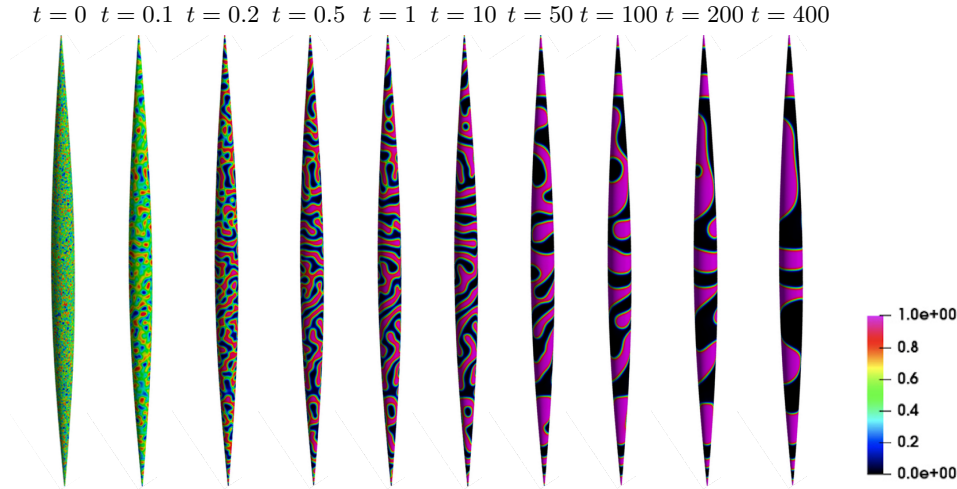


Fig. 4.13: Evolution of the numerical solution of the Cahn–Hilliard equation on the spindle for  $t \in (0, 400]$  computed on a mesh with size  $h = 0.026$ . Time step is  $\Delta t = 0.01$  for  $t \in (0, 1]$  and  $\Delta t = 1$  for  $t \in (1, 400]$ . The simulation was started with a random initial condition depicted in the leftmost panel. View:  $xy$ -plane.

tried anything other than random initial condition.

**4.4. Phase separation on an idealized cell.** In this example, the surface  $\Gamma$  is given by the zero of the following level set function taken from [28]:

$$\phi(\mathbf{x}) = \frac{1}{4}x_1^2 + x_2^2 + \frac{4x_3^2}{(1 + \frac{1}{2}\sin(\pi x_1))^2} - 1.$$

The surface is illustrated in Fig. 4.14 and can be viewed as an idealized cell. As mentioned in Sec. 3, our long term goal is to simulate phase separation on biological membranes that exhibit shape transitions and shape instabilities. Thus, we need to go beyond simple surfaces like the sphere and the spindle. Besides its more complex, amorphous shape, what distinguishes the surface of the idealized cell is that it is possible to trace a curve of minimal length on it. We shall see that this geometric property critically defines the equilibrium stage of the non-conservative evolution of lateral phase separation process.

The surface is embedded in an outer domain  $\Omega = [-2, 2] \times [-4/3, 4/3] \times [-4/3, 4/3]$ . The computational mesh  $\mathcal{T}_h^\Gamma$  of  $\Omega$  has mesh size  $h = 0.031$ . This tetrahedral mesh is generated in the same way as the meshes for the sphere and the spindle are generated, i.e. by diving  $\Omega$  into cubes and then diving the cubes into tetrahedra. The elements cut by the surface are further refined. This mesh has a level of refinement comparable to mesh  $\ell = 6$  in Sec. 4.1. We recall that the discrete surface  $\Gamma_h$  is implicitly defined by the zero set of  $\phi_{h/2} = I_{h/2}(\phi)$  and does not require any explicit parametrization of  $\Gamma$ . This makes our numerical approach particularly suitable for dealing with complex shapes. The resulting surface mesh, which is illustrated in Fig. 4.14 (b) for the entire  $\Gamma$  and in Fig. 4.15 for the ‘beak’ part of  $\Gamma$ , is used for numerical integration only, while test and trial finite element functions are defined on shape regular bulk tetrahedra.

We simulate phase separation on the idealized cell surface using the Allen–Cahn and Cahn–Hilliard models, i.e. eq. (2.4) and eq. (2.10), with free energy per unit surface

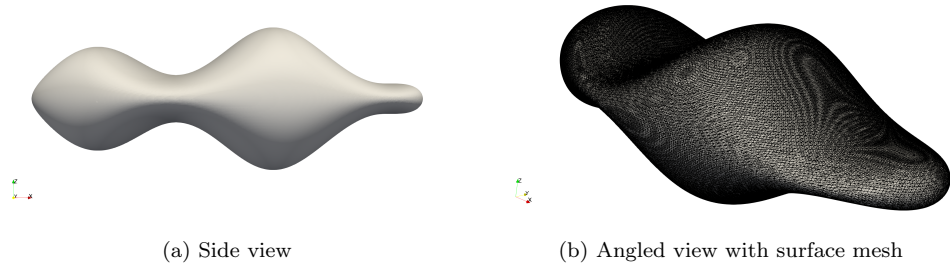


Fig. 4.14: Illustration of the surface of the idealized cell: (a) side view and (b) angled view with the trace surface for the mesh in use.

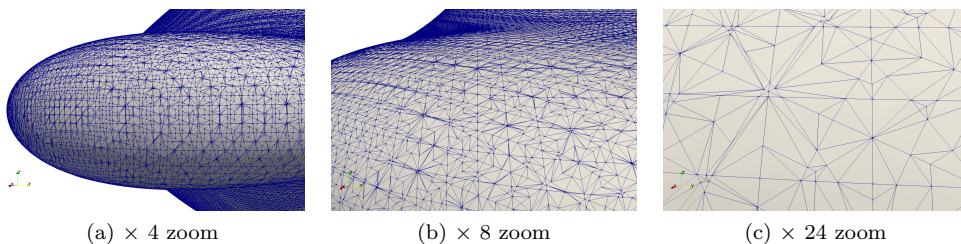


Fig. 4.15: Zoomed views the surface triangulation induced by embedding of the surface into the bulk tetrahedral mesh.

(2.14),  $\alpha = 1$ , and  $\epsilon = 0.01$ . Like for the sphere and the spindle, the initial condition is  $\eta_0(\mathbf{x}) = \text{rand}(\mathbf{x})$ .

**4.4.1. Allen–Cahn model.** First we apply Allen–Cahn model to simulate non-conservative evolution of phase separation. Fig. 4.16 shows the initial fast evolution of the numerical solution of the Allen–Cahn equation, followed by the beginning of the slowdown phase. In Fig. 4.17 we see the process of separation into two regions, one pink region with  $\eta = 1$  and one black region with  $\eta = 0$ . The separation itself occurs around  $t = 1600$ . Finally, Fig. 4.18 shows the evolution towards the steady state. After  $t = 20000$  there is no visible change in the position of the interface between phases, which virtually *coincided with the curve of minimal length* on  $\Gamma$ . The computed equilibrium state is consistent with the well-known limiting (as  $\epsilon \rightarrow 0$ ) behaviour of the Allen–Cahn model, which defines the evolution of the sharp interface as the mean curvature motion [37]. For the surface Allen–Cahn equation one obtains geodesic curvature motion of the interface in the asymptotic limit [33] with any closed geodesic as an equilibrium state. We note that for the given surface this equilibrium state is stable. Therefore, unlike the cases of the sphere and spindle, on the idealized cell neither phase vanishes.

Like for the sphere, we prescribe different time steps for the different stages of the phase separation. Table 4.1 reports the time step assigned for each time intervals.

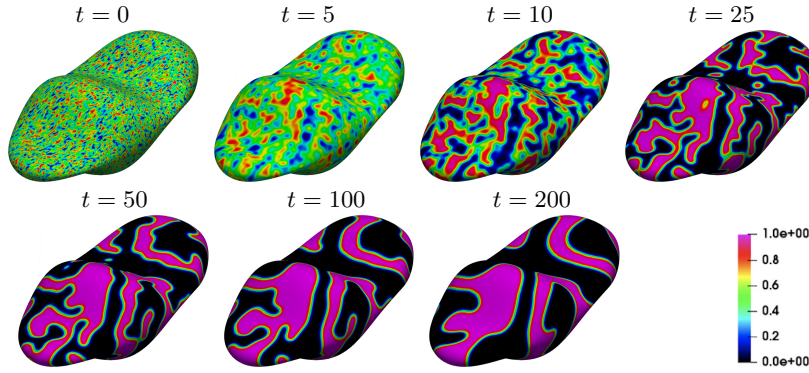


Fig. 4.16: Evolution of the numerical solution of the Allen–Cahn equation on the idealized cell surface for  $t \in (0, 200]$  computed with time step as specified in Table 4.2 and on a mesh with size  $h = 0.031$ . The simulation was started with a random initial condition depicted in the top left panel.

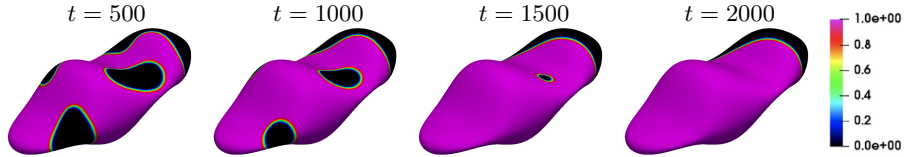


Fig. 4.17: Evolution of the numerical solution of the Allen–Cahn equation on the idealized cell surface for  $t \in [500, 2000]$  computed with time step as specified in Table 4.2 and on a mesh with size  $h = 0.031$ .

**4.4.2. Cahn–Hilliard model.** In the last subsection, we apply the Cahn–Hilliard model to simulate the conservative evolution of phase separation on the idealized cell. The evolution of the numerical solution to the Cahn–Hilliard equation for  $t \in [0, 1000]$  is shown in Fig. 4.19. Just like on the sphere and on the spindle, we see the initial fast phase that ends around  $t = 1$  and is followed by the slowdown phase. Thus, the time steps are chosen like for the tests on the sphere and on the spindle.

The evolution of the numerical solution for  $t \in [2000, 30000]$  is shown in Fig. 4.20. After  $t = 25000$ , we observe a further deceleration in the process of dissipation of the interfacial energy. This is even more evident in Fig. 4.21, which displays a side view of the solution for  $t \in [32000, 36000]$ . Since there is no visible change in the position of the interface between phases after  $t = 36000$ , we consider the rightmost panel in Fig. 4.21 close to the steady state. Just like for the sphere (see Sec. 4.2.2), we see one large and one small pink domain (i.e.,  $c = 1$ ): the small domain is positioned around the ‘beak’ and the large one is at the opposite end.

Finally, we note that although the shape of the surface clearly affects the steady state of the phases, its influence on the spinodal decomposition, initial and intermediate stages of phase separation is less evident from our results. This agrees with the limiting behavior of the models: interface motion by the geodesic curvature for the Allen–Cahn equation [33] and the minus Laplace–Beltrami operator of the geodesic curvature along the interface for the Cahn–Hilliard equation [18, 70]. Hence, the

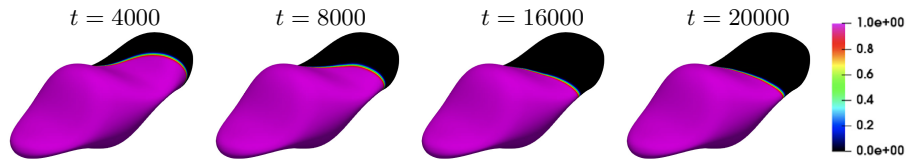


Fig. 4.18: Evolution of the numerical solution of the Allen–Cahn equation on the idealized cell surface for  $t \in [4000, 20000]$  computed with time step as specified in Table 4.2 and on a mesh with size  $h = 0.031$ .

interval	(0, 200]	(200, 500]	(500, 23000]
$\Delta t$	1	5	10

Table 4.2: Time steps used for the different time intervals to obtain the results Fig. 4.16, 4.17, and 4.18.

evolution of the interfaces between lateral phases is largely driven by their intrinsic curvature and the interplay with the membrane shape is not explicit.

**5. Conclusions.** We performed a computational study of lateral phase separation and coarsening on surfaces of biological interest. To model these processes, we considered both the Allen–Cahn (conservative model) and the Cahn–Hilliard (non-conservative model) equations posed on surfaces. Although in this work we assume the surfaces to be rigid, our longer term goal is to solve numerically the Allen–Cahn and Cahn–Hilliard equation on evolving shapes. In fact, biological membranes exhibit shape transitions and shape instabilities, which need to be accounted for in a realistic model. This need dictated our choice for the numerical approach.

We considered the trace finite element method (TraceFEM), which was shown in [57] to handle relatively easily evolving surfaces. TraceFEM is a geometrically unfitted method that has an important additional advantage: surfaces can be defined implicitly and no knowledge of the surface parametrization is required. This allows flexible numerical treatment of complex shapes, like the ones found in cell biology.

After validating the accuracy of our implementation of TraceFEM with benchmark problems, we applied it to simulate phase transition on a series of surfaces of increasing geometric complexity using both the surface Allen–Cahn and Cahn–Hilliard models. We compared the numerical results produced by the two models on a sphere and found that the Cahn–Hilliard model successfully reproduces the spinodal decomposition experimentally observed in giant vesicles in [81]. Both models were also compared on the surface of a spindle with the aim of getting a preliminary insight into the formation of microdomains in bacteria [15]. Finally, we presented the results on a more complex surface that represents an idealized cell. For both the sphere and the idealized cell, we let the simulations run until sufficiently close to the steady state to understand the role of certain geometric characteristics on the final equilibrium.

## REFERENCES

- [1] M. R. ADKINS AND Y. C. ZHOU, *Geodesic curvature driven surface microdomain formation*, J. Comput. Phys., 345 (2017), pp. 260–274.

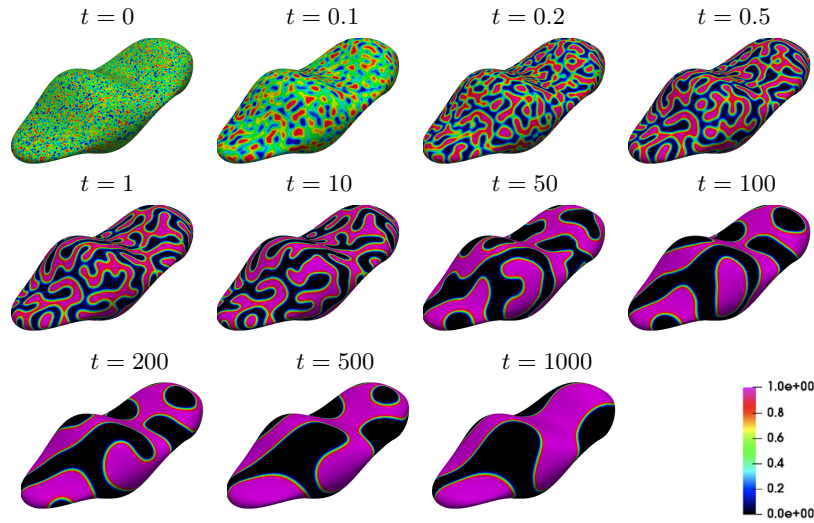


Fig. 4.19: Evolution of the numerical solution of the Cahn–Hilliard equation on the idealized cell surface for  $t \in (0, 1000]$  computed on a mesh with size  $h = 0.031$ . Time step is  $\Delta t = 0.01$  for  $t \in (0, 1]$  and  $\Delta t = 1$  for  $t \in (1, 1000]$ . The simulation was started with a random initial condition depicted in the top left panel.

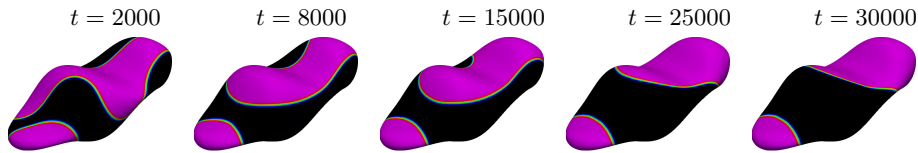


Fig. 4.20: Evolution of the numerical solution of the Cahn–Hilliard equation on the idealized cell surface for  $t \in [2000, 30000]$  computed on a mesh with size  $h = 0.031$  and with time step is  $\Delta t = 1$ . The legend is as in Fig. 4.19.

- [2] S. ALAND, S. EGERER, J. LOWENGRUB, AND A. VOIGT, *Diffuse interface models of locally inextensible vesicles in a viscous fluid*, Journal of Computational Physics, 277 (2014), pp. 32 – 47.
- [3] S. M. ALLEN AND J. W. CAHN, *A microscopic theory for antiphase boundary motion and its application to antiphase domain coarsening*, Acta Metallurgica, 27 (1979), pp. 1085 – 1095.
- [4] D. ANDELMAN, T. KAWAKATSU, AND K. KAWASAKI, *Equilibrium shape of two-component unilamellar membranes and vesicles*, EPL (Europhysics Letters), 19 (1992), p. 57.
- [5] D. M. ANDERSON, G. B. MCFADDEN, AND A. A. WHEELER, *Diffuse-interface methods in fluid mechanics*, Annual Review of Fluid Mechanics, 30 (1998), pp. 139–165.
- [6] G. S. AYTON, J. L. MCWHIRTER, P. MCMURTRY, AND G. A. VOTH, *Coupling field theory with continuum mechanics: a simulation of domain formation in giant unilamellar vesicles*, Biophysical journal, 88 (2005), pp. 3855–3869.
- [7] L. BAGATOLLI AND P. B. SUNIL KUMAR, *Phase behavior of multicomponent membranes: Experimental and computational techniques*, Soft Matter, 5 (2009), pp. 3234–3248.
- [8] L. BAÑAS AND R. NÜRNBERG, *Adaptive finite element methods for Cahn–Hilliard equations*, Journal of Computational and Applied Mathematics, 218 (2008), pp. 2–11.
- [9] A. BANDEKAR, C. ZHU, A. GOMEZ, M. Z. MENZENSKI, M. SEMPKOWSKI, AND S. SOFOU, *Masking and triggered unmasking of targeting ligands on liposomal chemotherapy selectively suppress tumor growth in vivo*, Molecular Pharmaceutics, 10 (2013), pp. 152–160.
- [10] J. W. BARRETT, H. GARCKE, AND R. NÜRNBERG, *Finite element approximation for the dynamics of fluidic two-phase biomembranes*, ESAIM: Mathematical Modelling and Numerical

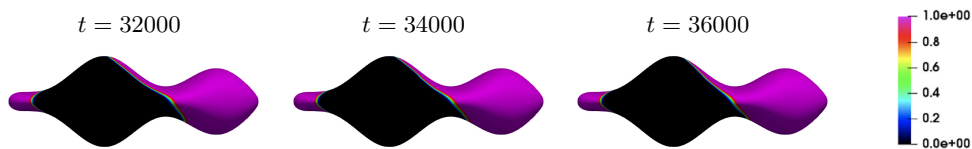


Fig. 4.21: Evolution of the numerical solution of the Cahn–Hilliard equation on the idealized cell surface for  $t \in [32000, 36000]$  computed on a mesh with size  $h = 0.031$  and with time step is  $\Delta t = 1$ . Side view.

- Analysis, 51 (2017), pp. 2319–2366.
- [11] T. BAUMGART, A. T. HAMMOND, P. SENGUPTA, S. T. HESS, D. A. HOLOWKA, B. A. BAIRD, AND W. W. WEBB, *Large-scale fluid/fluid phase separation of proteins and lipids in giant plasma membrane vesicles*, Proceedings of the National Academy of Sciences, 104 (2007), pp. 3165–3170.
- [12] T. BAUMGART, S. HESS, AND W. WEBB, *Imaging coexisting fluid domains in biomembrane models coupling curvature and line tension*, Nature, 425 (2003), pp. 821–824.
- [13] T. BAUMGART, G. HUNT, E. R. FARKAS, W. W. WEBB, AND G. W. FEIGENSON, *Fluorescence probe partitioning between lo/l<sub>d</sub> phases in lipid membranes*, Biochimica et Biophysica Acta (BBA) - Biomembranes, 1768 (2007), pp. 2182 – 2194.
- [14] W. J. BOETTINGER, J. A. WARREN, C. BECKERMANN, AND A. KARMA, *Phase-field simulation of solidification*, Annual review of materials research, 32 (2002), pp. 163–194.
- [15] M. BRAMKAMP AND D. LOPEZ, *Exploring the existence of lipid rafts in bacteria*, Microbiol. Mol. Biol. Rev., 79 (2015), pp. 81–100.
- [16] J. CAHN AND J. HILLIARD, *Free energy of a nonuniform system. i. interfacial free energy*, The Journal of Chemical Physics, 28 (1958), pp. 258–267.
- [17] J. W. CAHN, *On spinodal decomposition*, Acta Metallurgica, 9 (1961), pp. 795 – 801.
- [18] J. W. CAHN, C. M. ELLIOTT, AND A. NOVICK-COHEN, *The cahn-hilliard equation with a concentration dependent mobility: motion by minus the laplacian of the mean curvature*, European journal of applied mathematics, 7 (1996), pp. 287–301.
- [19] Y. CAI, H. CHOI, AND J. SHEN, *Error estimates for time discretizations of Cahn–Hilliard and Allen–Cahn phase-field models for two-phase incompressible flows*, Numerische Mathematik, 137 (2017), pp. 417–449.
- [20] B. A. CAMLEY AND F. L. H. BROWN, *Dynamic simulations of multicomponent lipid membranes over long length and time scales*, Phys. Rev. Lett., 105 (2010), p. 148102.
- [21] ———, *Dynamic scaling in phase separation kinetics for quasi-two-dimensional membranes*, J. Chem. Phys., 135 (2011), p. 225106.
- [22] L.-Q. CHEN, *Phase-field models for microstructure evolution*, Annual Review of Materials Research, 32 (2002), pp. 113–140.
- [23] A. H. DE VRIES, A. E. MARK, AND S. J. MARRINK, *Molecular dynamics simulation of the spontaneous formation of a small DPPC vesicle in water in atomistic detail*, Journal of the American Chemical Society, 126 (2004), pp. 4488–4489.
- [24] *DROPS package*. <http://www.igpm.rwth-aachen.de/DROPS/>.
- [25] Q. DU, L. JU, AND L. TIAN, *Finite element approximation of the Cahn–Hilliard equation on surfaces*, Computer Methods in Applied Mechanics and Engineering, 200 (2011), pp. 2458–2470.
- [26] Q. DU, C. LIU, AND X. WANG, *Simulating the deformation of vesicle membranes under elastic bending energy in three dimensions*, Journal of Computational Physics, 212 (2006), pp. 757–777.
- [27] G. DZIUK AND C. M. ELLIOTT, *Surface finite elements for parabolic equations*, Journal of Computational Mathematics, (2007), pp. 385–407.
- [28] ———, *Finite element methods for surface pdes*, Acta Numerica, 22 (2013), pp. 289–396.
- [29] M. EDIDIN, *The state of lipid rafts: From model membranes to cells*, Annual Review of Biophysics and Biomolecular Structure, 32 (2003), pp. 257–283.
- [30] ———, *The state of lipid rafts: from model membranes to cells*, Annual review of biophysics and biomolecular structure, 32 (2003), pp. 257–283.
- [31] C. M. ELLIOTT, D. A. FRENCH, AND F. MILNER, *A second order splitting method for the Cahn–Hilliard equation*, Numerische Mathematik, 54 (1989), pp. 575–590.



- [32] C. M. ELLIOTT AND T. RANNER, *Evolving surface finite element method for the Cahn–Hilliard equation*, Numerische Mathematik, 129 (2015), pp. 483–534.
- [33] C. M. ELLIOTT AND B. STINNER, *Modeling and computation of two phase geometric biomembranes using surface finite elements*, Journal of Computational Physics, 229 (2010), pp. 6585–6612.
- [34] C. M. ELLIOTT AND B. STINNER, *A surface phase field model for two-phase biological membranes*, SIAM J. Appl. Math., 70 (2010), pp. 2904–2928.
- [35] C. M. ELLIOTT AND B. STINNER, *Computation of two-phase biomembranes with phase dependent material parameters using surface finite elements*, Communications in Computational Physics, 13 (2013), pp. 325–360.
- [36] H. EMMERICH, *The Diffuse Interface Approach in Materials Science: Thermodynamic Concepts and Applications of Phase-Field Models*, Springer Publishing Company, Incorporated, 2011.
- [37] L. C. EVANS, H. M. SONER, AND P. E. SOUGANIDIS, *Phase transitions and generalized motion by mean curvature*, Communications on Pure and Applied Mathematics, 45 (1992), pp. 1097–1123.
- [38] X. FENG AND A. PROHL, *Error analysis of a mixed finite element method for the Cahn–Hilliard equation*, Numerische Mathematik, 99 (2004), pp. 47–84.
- [39] C. M. FUNKHOUSER, F. J. SOLIS, AND K. THORNTON, *Dynamics of two-phase lipid vesicles: effects of mechanical properties on morphology evolution*, Soft Matter, 6 (2010), pp. 3462–3466.
- [40] C. M. FUNKHOUSER, F. J. SOLIS, AND K. THORNTON, *Dynamics of coarsening in multicomponent lipid vesicles with non-uniform mechanical properties*, The Journal of Chemical Physics, 140 (2014), p. 144908.
- [41] H. GARCKE, J. KAMPMANN, A. RÄTZ, AND M. RÖGER, *A coupled surface–Cahn–Hilliard bulk–diffusion system modeling lipid raft formation in cell membranes*, Mathematical Models and Methods in Applied Sciences, 26 (2016), pp. 1149–1189.
- [42] P. GERA AND D. SALAC, *Cahn–Hilliard on surfaces: A numerical study*, Applied Mathematics Letters, 73 (2017), pp. 56–61.
- [43] H. GOMEZ AND T. J. HUGHES, *Provably unconditionally stable, second-order time-accurate, mixed variational methods for phase-field models*, Journal of Computational Physics, 230 (2011), pp. 5310 – 5327.
- [44] J. GRANDE, C. LEHRENFELD, AND A. REUSKEN, *Analysis of a high-order trace finite element method for pdes on level set surfaces*, SIAM Journal on Numerical Analysis, 56 (2018), pp. 228–255.
- [45] J. B. GREER, A. L. BERTOZZI, AND G. SAPIRO, *Fourth order partial differential equations on general geometries*, Journal of Computational Physics, 216 (2006), pp. 216–246.
- [46] F. GUILLÉN-GONZÁLEZ AND G. TIERRA, *Second order schemes and time-step adaptivity for Allen–Cahn and Cahn–Hilliard models*, Computers & Mathematics with Applications, 68 (2014), pp. 821–846.
- [47] J. L. HARDEN AND F. C. MACKINTOSH, *Shape transformations of domains in mixed-fluid films and bilayer membranes*, EPL (Europhysics Letters), 28 (1994), p. 495.
- [48] T. HOU, K. WANG, Y. XIONG, X. XIAO, AND S. ZHANG, *Discrete maximum-norm stability of a linearized second-order finite difference scheme for Allen–Cahn equation*, Numerical Analysis and Applications, 10 (2017), pp. 177–183.
- [49] J. H. HURLEY, E. BOURA, L.-A. CARLSON, AND B. RYCKI, *Membrane budding*, Cell, 143 (2010), pp. 875 – 887.
- [50] D. JEONG AND J. KIM, *Microphase separation patterns in diblock copolymers on curved surfaces using a nonlocal Cahn–Hilliard equation*, The European Physical Journal E, 38 (2015), p. 117.
- [51] S. KARVE, A. BANDEKAR, M. R. ALI, AND S. SOFOU, *The ph-dependent association with cancer cells of tunable functionalized lipid vesicles with encapsulated doxorubicin for high cell-kill selectivity*, Biomaterials, 31 (2010), pp. 4409 – 4416.
- [52] T. KAWAKATSU, D. ANDELMAN, K. KAWASAKI, AND T. TANIGUCHI, *Phase transitions and shapes of two component membranes and vesicles i: strong segregation limit*, J. Phys. II France, 3 (1993), pp. 971–997.
- [53] J. KIM, D. JEONG, S.-D. YANG, AND Y. CHOI, *A finite difference method for a conservative Allen–Cahn equation on non-flat surfaces*, Journal of Computational Physics, 334 (2017), pp. 170–181.
- [54] L. LANDAU AND E. LIFSHITZ, *Statistical physics*, Oxford: Pergamon, 1958.
- [55] A. LAOUINI, C. JAAFAR-MAALEJ, I. LIMAYEM-BLOUZA, S. SFAR, C. CHARCOSSET, AND H. FESSI, *Preparation, characterization and applications of liposomes: State of the art*, Journal of

- Colloid Science and Biotechnology, 1 (2012), pp. 147–168.
- [56] M. LARADJI AND P. B. SUNIL KUMAR, *Dynamics of domain growth in self-assembled fluid vesicles*, Phys. Rev. Lett., 93 (2004), p. 198105.
- [57] C. LEHRENFELD, M. A. OLSHANSKII, AND X. XU, *A stabilized trace finite element method for partial differential equations on evolving surfaces*, SIAM Journal on Numerical Analysis, 56 (2018), pp. 1643–1672.
- [58] S. LI, J. LOWENGRUB, AND A. VOIGT, *Locomotion, wrinkling, and budding of a multicomponent vesicle in viscous fluids*, Communications in Mathematical Sciences, 10 (2012), p. 645670.
- [59] Y. LI, J. KIM, AND N. WANG, *An unconditionally energy-stable second-order time-accurate scheme for the Cahn–Hilliard equation on surfaces*, Communications in Nonlinear Science and Numerical Simulation, 53 (2017), pp. 213–227.
- [60] C. LIU AND J. SHEN, *A phase field model for the mixture of two incompressible fluids and its approximation by a fourier-spectral method*, Physica D: Nonlinear Phenomena, 179 (2003), pp. 211 – 228.
- [61] F. LIU AND J. SHEN, *Stabilized semi-implicit spectral deferred correction methods for Allen–Cahn and Cahn–Hilliard equations*, Mathematical Methods in the Applied Sciences, 38 (2015), pp. 4564–4575.
- [62] J. LOWENGRUB, A. RÄTZ, AND A. VOIGT, *Phase-field modeling of the dynamics of multicomponent vesicles: Spinodal decomposition, coarsening, budding, and fission*, Physical review. E, Statistical, nonlinear, and soft matter physics, 79 (2009), p. 031926.
- [63] J. LOWENGRUB AND L. TRUSKINOVSKY, *Quasi-incompressible Cahn–Hilliard fluids and topological transitions*, Proceedings of the Royal Society of London A: Mathematical, Physical and Engineering Sciences, 454 (1998), pp. 2617–2654.
- [64] R. E. MAGI AND J. P. KEENER, *Modelling a biological membrane as a two phase viscous fluid with curvature elasticity*, SIAM Journal on Applied Mathematics, 77 (2017), pp. 128–153.
- [65] S. J. MARRINK AND A. E. MARK, *Molecular dynamics simulation of the formation, structure, and dynamics of small phospholipid vesicles*, Journal of the American Chemical Society, 125 (2003), pp. 15233–15242.
- [66] J. L. MCWHIRTER, G. AYTON, AND G. A. VOTH, *Coupling field theory with mesoscopic dynamical simulations of multicomponent lipid bilayers*, Biophysical journal, 87 (2004), pp. 3242–3263.
- [67] M. MERCKER, M. PTASHNYK, J. KÜHNLE, D. HARTMANN, M. WEISS, AND W. JÄGER, *A multiscale approach to curvature modulated sorting in biological membranes*, Journal of theoretical biology, 301 (2012), pp. 67–82.
- [68] S. MUNRO, *Lipid rafts: elusive or illusive?*, Cell, 115 (2003), pp. 377–388.
- [69] I. NITSCHKE, A. VOIGT, AND J. WENSCH, *A finite element approach to incompressible two-phase flow on manifolds*, Journal of Fluid Mechanics, 708 (2012), p. 418438.
- [70] D. O’CONNOR AND B. STINNER, *The cahn-hilliard equation on an evolving surface*, arXiv preprint arXiv:1607.05627, (2016).
- [71] M. A. OLSHANSKII AND A. REUSKEN, *Trace finite element methods for pdes on surfaces*, in Geometrically Unfitted Finite Element Methods and Applications, Springer, 2017, pp. 211–258.
- [72] M. A. OLSHANSKII, A. REUSKEN, AND J. GRANDE, *A finite element method for elliptic equations on surfaces*, SIAM J. Numer. Anal., 47 (2009), pp. 3339–3358.
- [73] J. P. SCHLEBACH, P. J. BARRETT, C. A. DAY, J. H. KIM, A. K. KENWORTHY, AND C. R. SANDERS, *Topologically diverse human membrane proteins partition to liquid-disordered domains in phase-separated lipid vesicles*, Biochemistry, 55 (2016), pp. 985–988.
- [74] U. SEIFERT, *Curvature-induced lateral phase segregation in two-component vesicles*, Phys. Rev. Lett., 70 (1993), pp. 1335–1338.
- [75] J. SHEN, T. TANG, AND J. YANG, *On the maximum principle preserving schemes for the generalized Allen–Cahn equation*, Commun. Math. Sci., 14 (2016), p. 15171534.
- [76] J. SHEN AND X. YANG, *Numerical approximations of Allen–Cahn and Cahn–Hilliard equations*, Discrete & Continuous Dynamical Systems - A, 28 (2010), p. 1669.
- [77] K. SIMONS AND E. IKONEN, *Functional rafts in cell membranes*, Nature, 387 (1997), p. 569.
- [78] J. S. SOHN, Y.-H. TSENG, S. LI, A. VOIGT, AND J. S. LOWENGRUB, *Dynamics of multicomponent vesicles in a viscous fluid*, Journal of Computational Physics, 229 (2010), pp. 119–144.
- [79] T. TANIGUCHI, K. KAWASAKI, D. ANDELMAN, AND T. KAWAKATSU, *Phase transitions and shapes of two component membranes and vesicles ii : weak segregation limit*, J. Phys. II France, 4 (1994), pp. 1333–1362.
- [80] G. TIERRA AND F. GUILLÉN-GONZÁLEZ, *Numerical methods for solving the Cahn–Hilliard equation and its applicability to related energy-based models*, Archives of Computational Methods in Engineering, 22 (2015), pp. 269–289.

- [81] S. L. VEATCH AND S. L. KELLER, *Separation of liquid phases in giant vesicles of ternary mixtures of phospholipids and cholesterol*, Biophysical Journal, 85 (2003), pp. 3074 – 3083.
- [82] X. WANG AND Q. DU, *Modelling and simulations of multi-component lipid membranes and open membranes via diffuse interface approaches*, Journal of Mathematical Biology, 56 (2008), pp. 347–371.
- [83] T. WITKOWSKI, R. BACKOFEN, AND A. VOIGT, *The influence of membrane bound proteins on phase separation and coarsening in cell membranes*, Phys. Chem. Chem. Phys., 14 (2012), pp. 14509–14515.
- [84] O. WODO AND B. GANAPATHYSUBRAMANIAN, *Computationally efficient solution to the Cahn-Hilliard equation: Adaptive implicit time schemes, mesh sensitivity analysis and the 3d isoperimetric problem*, Journal of Computational Physics, 230 (2011), pp. 6037 – 6060.
- [85] P. YUE, C. ZHOU, J. J. FENG, C. F. OLLIVIER-GOOCH, AND H. H. HU, *Phase-field simulations of interfacial dynamics in viscoelastic fluids using finite elements with adaptive meshing*, Journal of Computational Physics, 219 (2006), pp. 47–67.
- [86] Z. ZHANG AND Z. QIAO, *An adaptive time-stepping strategy for the Cahn-Hilliard equation*, Communications in Computational Physics, 11 (2012), p. 12611278.
- [87] J. ZHU, L.-Q. CHEN, J. SHEN, AND V. TIKARE, *Coarsening kinetics from a variable-mobility Cahn-Hilliard equation: Application of a semi-implicit Fourier spectral method*, Phys. Rev. E, 60 (1999), pp. 3564–3572.